A&A 418, 827–840 (2004)
DOI: 10.1051/0004-6361:20035622

Astronomy & Astrophysics

The HELLAS2XMM survey

V. Near-Infrared observations of X-ray sources with *extreme* X/O ratios⋆

M. Mignoli[1], L. Pozzetti[1], A. Comastri[1], M. Brusa[1,2], P. Ciliegi[1], F. Cocchia[3], F. Fiore[3], F. La Franca[4], R. Maiolino[5], G. Matt[4], S. Molendi[6], G.C. Perola[4], S. Puccetti[3], P. Severgnini[7], and C. Vignali[1]

[1] INAF-Osservatorio Astronomico di Bologna, via Ranzani 1, 40127 Bologna, Italy
e-mail: lucia,comastri,ciliegi,l_vignali@bo.astro.it
[2] Dipartimento di Astronomia Università di Bologna, via Ranzani 1, 40127 Bologna, Italy
e-mail: brusa@bo.astro.it
[3] INAF-Osservatorio Astronomico di Roma, via Frascati 33, 00040 Monteporzio, Italy
e-mail: cocchia,fiore,puccetti@mporzio.astro.it
[4] Dipartimento di Fisica Università di Roma Tre, via Vasca Navale 84, 00146 Roma, Italy
e-mail: lafranca,matt,perola@fis.uniroma3.it
[5] INAF-Osservatorio Astrofisico di Arcetri, Largo E. Fermi 5, 50125, Firenze, Italy
e-mail: maiolino@arcetri.astro.it
[6] IASF-CNR, Istituto di Fisica Cosmica, via Bassini 15, 20133, Milano, Italy
e-mail: silvano@mi.iasf.cnr.it
[7] INAF-Osservatorio Astronomico di Brera, via Brera 28, 20121 Milano, Italy
e-mail: paola@brera.mi.astro.it

Received 3 November 2003 / Accepted 19 January 2004

Abstract. We present the results of deep near-infrared observations (with ISAAC at VLT) of eleven hard X-ray selected sources in the Hellas2XMM survey, with faint optical magnitude ($R \gtrsim 24$) and high X-ray-to-optical flux ratio. All but one of the sources have been detected in the K_s band, with bright counterparts ($K_s < 19$) and very red colors ($R - K > 5$), and therefore belong to the ERO population. The quality of the near-infrared data is such that we can take advantage of the sub-arcsec seeing to obtain accurate morphological information. A detailed analysis of the surface brightness profiles allows us to classify all of the near-infrared counterparts. There are two point-like objects, seven elliptical (bulge) galaxies and one source with an exponential profile. None of the extended sources shows any evidence of the presence of a central unresolved object tracing the putative X-ray emitting AGN. Using both the $R - K$ colors and the morphological information, we have estimated for all the sources a "minimum photometric redshift", ranging between 0.8 and 2.4; the elliptical hosts have $z_{\rm min} = 0.9-1.4$. We computed the X-ray properties using these redshifts: most of the sources have $N_{\rm H} > 10^{22}$ cm^{-2}, with unabsorbed X-ray luminosities up to 10^{45} erg s^{-1} in the intrinsic 2−10 keV band. These objects therefore belong to the long-sought population of obscured (type II) quasars and, from a statistical point of view, they are a non-negligible fraction (about 10%) of the most luminous AGN. Selecting the high X/O sources for a follow-up study in the near-infrared is therefore a powerful technique aimed at studying at high redshift the hosts of Type II AGN, whose obscured nuclei do not affect the host galaxy morphologies. Overall, our results seem to indicate that the hosts are mostly elliptical galaxies at $z \sim 1$, and that these near-IR bright objects would be among the most massive spheroids at these epochs.

Key words. cosmology: observations – galaxies: active – infrared: galaxies – X-rays: galaxies

1. Introduction

With the advent of imaging X-ray telescopes operating onboard *Chandra* and XMM-*Newton*, a large fraction (>80%, Alexander et al. 2003; Giacconi et al. 2002; Hasinger et al. 2001; Mushotzky et al. 2000) of the Cosmic X-ray Background (XRB) in the 2−8 keV band has been resolved into discrete sources. The detailed study of the nature of the hard X-ray source population is pursued combining deep (1−2 Ms) *Chandra* pencil beam observations in the CDF-N and CDF-S,

Send offprint requests to: M. Mignoli,
e-mail: mignoli@bo.astro.it

⋆ Based on observations collected at the European Southern Observatory, Paranal, Chile (ESO Programme 70.A-0657) and La Silla, Chile (ESO Programme IDs: 66.A-0520, 67.A-0401, 68.A-0514). Based also on observations made with the XMM-*Newton*, an ESA science mission with instruments and contributions directly funded by ESA member states and the USA (NASA).

with shallower large area surveys (i.e. Hellas2XMM – Baldi et al. 2002; Champ – Green et al. 2003; SEXSI – Harrison et al. 2003). There are several issues which can be properly addressed only by surveying several square degrees at relatively bright fluxes, namely: i) the search for rare objects, which requires sufficiently wide areas to be discovered, ii) a more uniform coverage of the Hubble diagram and iii) a detailed study – by means of X-ray spectroscopy and/or by multi-wavelength follow-up – of X-ray sources which in the deep surveys are too faint for a similar approach.

In this respect we note that an interesting new population of X-ray sources is present in both the deep and shallow surveys. These objects are characterized by values of their X-ray-to-optical flux ratio $f_{\rm X-ray}/f_{\rm opt} > 10$ (hereinafter X/O; see Maccacaro et al. 1988 for a definition), which are significantly larger than those observed for soft X-ray selected AGN in the ROSAT surveys ($0.1 < {\rm X/O} < 10$; Lehmann et al. 2001; Zamorani et al. 1999). Almost by definition, sources with X/O > 10 have faint optical magnitudes. This is even more true for the faint X-ray sources discovered in the *Chandra* deep fields. For example, a 2–8 keV flux of $10^{-15}(10^{-16})$ erg cm^{-2} s^{-1} and an X/O ratio ∼10 correspond to R magnitudes ∼25.5 (∼28), challenging (well beyond) the spectroscopic capabilities of the 10 m-class telescopes.

On the other hand, at the brighter fluxes covered by the Hellas2XMM survey ($1–40 \times 10^{-14}$ erg cm^{-2} s^{-1}), the magnitudes of the optical counterparts of high X/O sources are of the order of $R \simeq 24$ or brighter, making spectroscopic follow-up observations feasible. Indeed, more than half of the Hellas2XMM sources with X/O > 10, for which good quality VLT spectra are available, are classified as type II QSOs on the basis of the lack of broad optical lines and high X-ray luminosity ($L_{2-10\ {\rm keV}} > 10^{44}$ erg s^{-1}; see Fiore et al. 2003). It seems reasonable to argue that most of the sources characterized by a high value of X/O are high redshift, obscured AGN. If this were the case, they could contribute to reducing the disagreement between the redshift distribution predicted by XRB synthesis models and that observed in deep *Chandra* and XMM-*Newton* fields (Hasinger 2003; Gilli 2003), and provide an important contribution to the total energy density of the background light. Furthermore, sources with even more extreme values of X/O (≫10) are present in the Hellas2XMM survey. These objects are again very challenging to be followed-up with the optical spectrographs attached to 10-m class telescopes, as they are both very faint ($R \gtrsim 25$) and spread over a large area of sky, making unfeasible any deep exposures with multi-object instruments. An alternative approach is to make use of the observed property that the optically fainter X-ray selected sources have, on average, redder colours (Giacconi et al. 2001; Lehmann et al. 2001; Alexander et al. 2002). This motivates the choice of the near infrared as the natural band to carry out a follow-up study of high X/O sources.

On the basis of these considerations, we started a pilot study in the $K_{\rm s}$ band, selecting a restricted but meaningful sample of Hellas2XMM sources that satisfy a well defined selection criterion: bright X-ray fluxes ($F(2-10\ {\rm keV}) > 10^{-14}$ erg cm^{-2} s^{-1}), high X-ray-to-optical flux ratios (X/O > 10) and no detection in the R band (see Fig. 1).

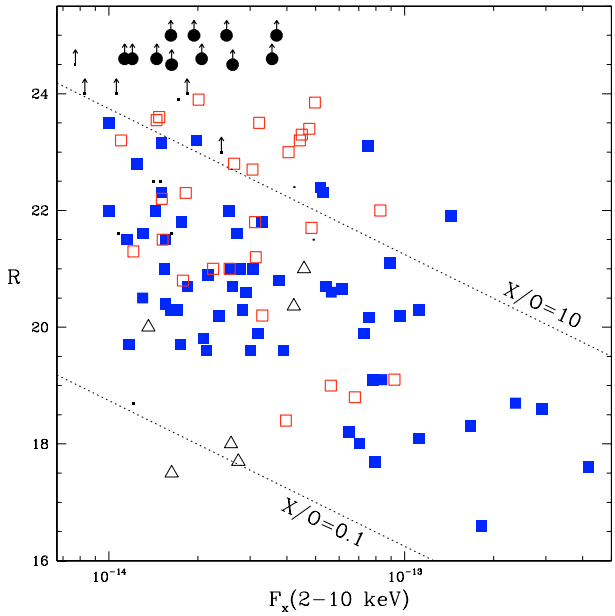

Fig. 1. The optical (R band) magnitude versus the X-ray (2–10 keV) flux for the Hellas2XMM 1dF sample. Different symbols identify different source classes: filled squares = broad line AGN; empty squares = narrow line AGN; triangles = early-type galaxies; small dot = spectroscopically unidentified sources. The selected sources observed with *ISAAC* are marked with large dots. The dotted lines indicate the loci of constant X-ray-to-optical flux ratio, delimiting the region of "conventional" AGN.

In Sect. 2 we present the target selection. The infrared data analysis and properties of the counterparts are discussed in Sects. 3 and 4, respectively. The results are presented in Sect. 5 and summarized in Sect. 6. A concordance cosmological model, with $H_0 = 70$ km s^{-1} Mpc^{-1}, $\Omega_m = 0.3$, $\Omega_\Lambda = 0.7$, is assumed throughout the paper.

2. The *Hellas2XMM* survey and the selection of the X-ray targets

The Hellas2XMM survey is a program of multiwavelength follow-up observations of hard X-ray selected sources serendipitously discovered in XMM-*Newton* fields over ∼4 deg^2. All the details on X-ray data analysis and source detection procedure have been already discussed in Baldi et al. (2002). To date, we have performed a complete optical follow-up program in five XMM-*Newton* fields covering a total of about 0.9 square degrees (the Hellas2XMM-1dF, Fiore et al. 2003). For all of the 122 sources in the Hellas2XMM-1dF sample we obtained relatively deep ($R = 24–25$) imaging using the ESO 3.6 m and the TNG telescopes; 106 sources (87%) were found to be associated with optical counterparts brighter than $R = 24$. For 97 objects redshift and classification have been obtained using ESO spectrographs (EFOSC2@3.6 m and FORS1@VLT/UT1). The source breakdown is summarized in Fig. 1 (see Brusa et al. 2003; Fiore et al. 2003 for all the details concerning the imaging and spectroscopic observations and the optical identification process).

Table 1. X-ray properties of the selected sources.

Source Id.	RA (J2000)	Dec (J2000)	2–10 keV flux (10^{-14} erg cm^{-2} s^{-1})	log(X/O)
Abell 2690 #075	23 59 56.6	−25 10 20	2.1 ± 0.7	>1.65
Abell 2690 #029	00 01 11.6	−25 12 03	3.6 ± 0.9	>1.89
BPM 16274 #069	00 50 30.7	−52 00 46	2.6 ± 0.5	>1.72
BPM 16274 #181	00 50 31.6	−52 06 30	1.6 ± 0.3	>1.50
PKS 0312-77 #045	03 10 19.0	−76 59 58	1.9 ± 0.6	>1.79
PKS 0312-77 #031	03 11 13.9	−76 53 59	1.2 ± 0.3	>1.42
PKS 0312-77 #036	03 13 43.5	−76 54 26	1.5 ± 0.5	>1.50
PKS 0537-28 #111	05 39 11.5	−28 37 18	3.7 ± 0.6	>2.19
PKS 0537-28 #054	05 39 45.3	−28 49 11	1.6 ± 0.5	>1.71
PKS 0537-28 #091	05 40 21.2	−28 50 38	2.5 ± 0.7	>2.06
PKS 0537-28 #037	05 41 00.4	−28 39 05	4.9 ± 1.3	>1.80

The majority of the unidentified sources (upward arrows in Fig. 1) are optically faint and are characterized by X/O > 10. The eleven X-ray brightest sources undetected in the optical with $R > 24.5$, were selected to be observed in the K_s band (shown in Fig. 1 as large dots in the upper part of the diagram). Most of them have a hard X-ray spectrum (see Sect. 5.3), lending further support to the hypothesis that they are obscured at both X-ray and optical wavelengths. The basic properties of the selected sample are given in Table 1.

3. Observations and data analysis

3.1. Near-infrared observations

Deep K_s[1] observations were obtained with the Infrared Spectrometer And Array Camera (*ISAAC*, see Moorwood et al. 1999) mounted on the ESO VLT-UT1 (*Antu*) telescope. *ISAAC* is equipped with a Rockwell Hawaii 1024 × 1024 HgCdTe array, with a pixel scale of 0.147″/pixel and a field of view of 2.′5 × 2.′5. The observations were collected in service mode over several nights in September 2002 under good seeing conditions (<0.″8). All the 11 fields were imaged with the same observing strategy, using the standard "auto-jitter" mode with the telescope being randomly offset by amounts of up to 30″ between individual short exposures for optimal background subtraction. Individual exposures have integration times of 6 × 10 s (n.sub-integrations × detector integration times), and each X-ray source field was imaged with 36 such jittered individual exposures for a common total integration time of 2160 s. The ESO calibration plan for *ISAAC* provides the necessary calibrations for our purposes, including detector darks, twilight flats and nightly photometric zero points, which were obtained by observing near-IR standard stars from the list of Persson et al. (1998).

The data reduction was performed in two stages: individual raw frames were first corrected for bias and dark current by subtracting a median dark frame, and flat-fielded using an average differential sky flat-field image. For the sky subtraction and image co-adding we used `DIMSUM`[2], a contributed package of IRAF[3]. To subtract the background, `DIMSUM` follows a two-step procedure. In the first step, a median sky is computed for each individual image from the six adjacent frames. The shifts between the sky-subtracted images are then computed and all of the frames are stacked to produce a "raw" co-added image. This image is used to build an object mask, which is used to flag the pixels belonging to sources in the individual frames. The second step repeats the operations of the first one, but includes the object masking and a rejection algorithm to remove cosmic rays. The final co-added images show flat, zero-leveled backgrounds and stable PSFs over the field of view. In Table 2 we summarize the relevant information of the K_s observations.

Object detection was carried out running `SExtractor` (Bertin & Arnouts 1996) on the final co-added images. Thanks to the high uniformity of the observations (see Table 2), we could use the same detection criterion for all of the data: we first convolved the data with a 0.″6-diameter Gaussian kernel and then classified as detected objects those with at least 5 connected pixels above 2.5 times the sky noise. As a measure of the *total* source magnitude we adopted the Kron-like magnitude, calculated by `SExtractor` by fitting elliptical "adaptive" apertures to each detection. The magnitudes are given in the Vega system. The star/galaxy classification was performed using a plot of the half-flux radius versus the K_s magnitude. Point-like objects are easily identified down to $K_s \simeq 19.0$, while the fainter objects were assumed to be galaxies: at these faint magnitudes and at high Galactic latitudes, the stellar contamination is negligible. The final catalog contains ≈1800 galaxies up to $K_s = 21.5$ in the area spanned by the *ISAAC* observations of ≈70 arcmin^2 (the edges of the mosaics were discarded because of the low signal-to-noise ratio). The galaxy counts agree well with the K20 survey counts (Cimatti et al. 2002a), and the comparison

[1] The K_s (*K short*) filter is centered at shorter wavelength than the standard K filter in order to reduce thermal background.

[2] Deep Infrared Mosaicing Software, developed by P. Eisenhardt, M. Dickinson, A. Stanford and J. Ward.

[3] IRAF is distributed by the National Optical Astronomy Observatories, which is operated by the Association of Universities for Research in Astronomy, Inc, under contract with the National Science Foundation.

Table 2. K_s observations characteristics.

Source Id.	Airmass	Seeing[a]	σ_μ(sky)[b]
Abell 2690 #075	1.39	0.58	22.09
Abell 2690 #029	1.17	0.49	21.92
BPM 16274 #069	1.16	0.76	22.17
BPM 16274 #181	1.24	0.76	22.19
PKS 0312-77 #045	2.00	0.61	21.95
PKS 0312-77 #031	1.63	0.56	21.91
PKS 0312-77 #036	1.84	0.63	22.01
PKS 0537-28 #111	1.97	0.47	22.00
PKS 0537-28 #054	1.47	0.38	22.08
PKS 0537-28 #091	1.57	0.57	22.10
PKS 0537-28 #037	1.28	0.53	22.13

[a] *FWHM* in arcsec.
[b] 1σ sky fluctuations in mag/arcsec^2.

with deeper surveys (Saracco et al. 2001; Bershady et al. 1998; Moustakas et al. 1997) suggests that we reach a 50% completeness at $K_s \approx 21$. The known discrepancy in the near-infrared surface density of galaxies between different surveys, to be mainly ascribed to cosmic variance, is also present in our data, where we find a factor up to ∼1.8 between the surface densities at $K_s = 20$ in different fields. This result is not at variance with the above statement of high uniformity in our data, since we must also take into account the nature of our targets, probably obscured and powerful AGN, and the known overdensity of near-infrared sources around high-z quasars (Hall & Green 1998). Finally, the incompleteness at faint magnitudes is not a drawback for this study, since all of the counterparts of our hard X-ray selected sources are bright in the near infrared, with $K_s \ll 20$ (see Sect. 4.1).

3.2. Optical imaging and source cross-matching

The optical imaging (*R-Bessel* filter) complementary to our deep near-infrared observations was obtained during two runs using EFOSC2 at the ESO 3.6 m telescope, in December 2000 and August 2001. Typical exposure times were about 10 min per field. The images were reduced using standard IRAF routines. For each observing run, we obtained the proper bias by combining several bias frames with a median filter. The images were then corrected for pixel to pixel response variations using the median of several flat-field frames obtained during the night. Cosmic rays and bad pixel corrections were applied to each frame. The photometric calibration was performed for each night using the zero-point derived from the measured instrumental magnitudes of standard stars and assuming the average extinction reported in the Observatory web pages[4]. Object detection was performed using `SExtractor`. Since the images were obtained under different seeing conditions (from 1.″1 to 2.″1), we used different threshold values from image to image so that the faintest detectable sources in all frames have a minimum signal-to-noise ratio of 3 over the seeing disk. Using these detection parameters, none of the hard X-ray selected sources discussed here was detected in the R band, and the limiting magnitude was estimated for each of them as the 3σ value over 2.5 times the seeing area. These limiting magnitudes ($24.5 < R_{\rm lim} < 25.2$) were adopted to compute the lower limits of X/O reported in Table 1. All of the magnitudes were corrected for Galactic extinction using the values from the NED Galactic extinction calculator[5] based upon the maps of Schlegel et al. (1998), although the extinction is generally small in our fields.

In order to cross match the near-infrared and optical catalogs, we elected as reference the K_s filter. First, we positionally registered the R images to the K_s mosaics, using ≈10−15 bright compact objects (mainly stars) for each frame. After having brought the two independently produced catalogs to a common astrometric reference, for each entry in the K_s catalog, we searched for objects closer than 2″ in the R catalog. In 80% of the cases we found an R-counterpart for entries brighter than $K_s = 20.5$ in the near-infrared catalog: the mean offset is consistent with zero, while the typical rms of the position differences in both right ascension and declination are of the order of 0.4″. At this stage we can confidently measure the colors of the galaxies in fixed apertures of 3″-diameter. We first degraded the seeing of the K_s images to that of the R band one, then we measured aperture magnitudes on both the R and K_s images (using the IRAF task `PHOT`) at the position given by the original detections on *ISAAC* data. With this method we increased the percentage of K_s entries with a measured $R - K$ color with respect to simply cross-correlating the two independently produced catalogs. Most important, we can measure, although with large errors, the R magnitude for a fraction of the K_s-detected counterparts of our X-rays targets. These sources were originally absent from the optical catalog, being just below the detection threshold limits.

4. Properties of the IR counterparts

4.1. Candidates identification and reliability

On the basis of the optical identification of the whole `Hellas2XMM` survey (Fiore et al. 2003; Brusa et al. 2003), we know that all of the counterparts of our X-ray sources are within 6″ from the XMM-*Newton* position (actually within 3″ for ∼80% of the cases). We therefore searched in the K_s catalog for objects closer than 6″ to the X-ray position: *in 10 out of 11 cases we found a relatively bright ($K_s \le 19$) near-infrared source well within the error circle* (see Fig. 2). The bright near-infrared counterparts have optical to near-infrared colors considerably redder than the field population; indeed, all of them are classified as Extremely Red Objects (EROs, with $R - K > 5$). The only exception is PKS0537-28 #037, where no object is detected within the error box, but several relatively bright galaxies, with similar $R - K$ colors, are present at distances less than 10″ from the nominal X-ray position: in this case the X-ray flux is probably due to thermal emission from the hot intragroup gas. Nevertheless, we cannot exclude the

[4] `http://www.eso.org/observing/support.html`

[5] `http://nedwww.ipac.caltech.edu/forms/calculator.html`

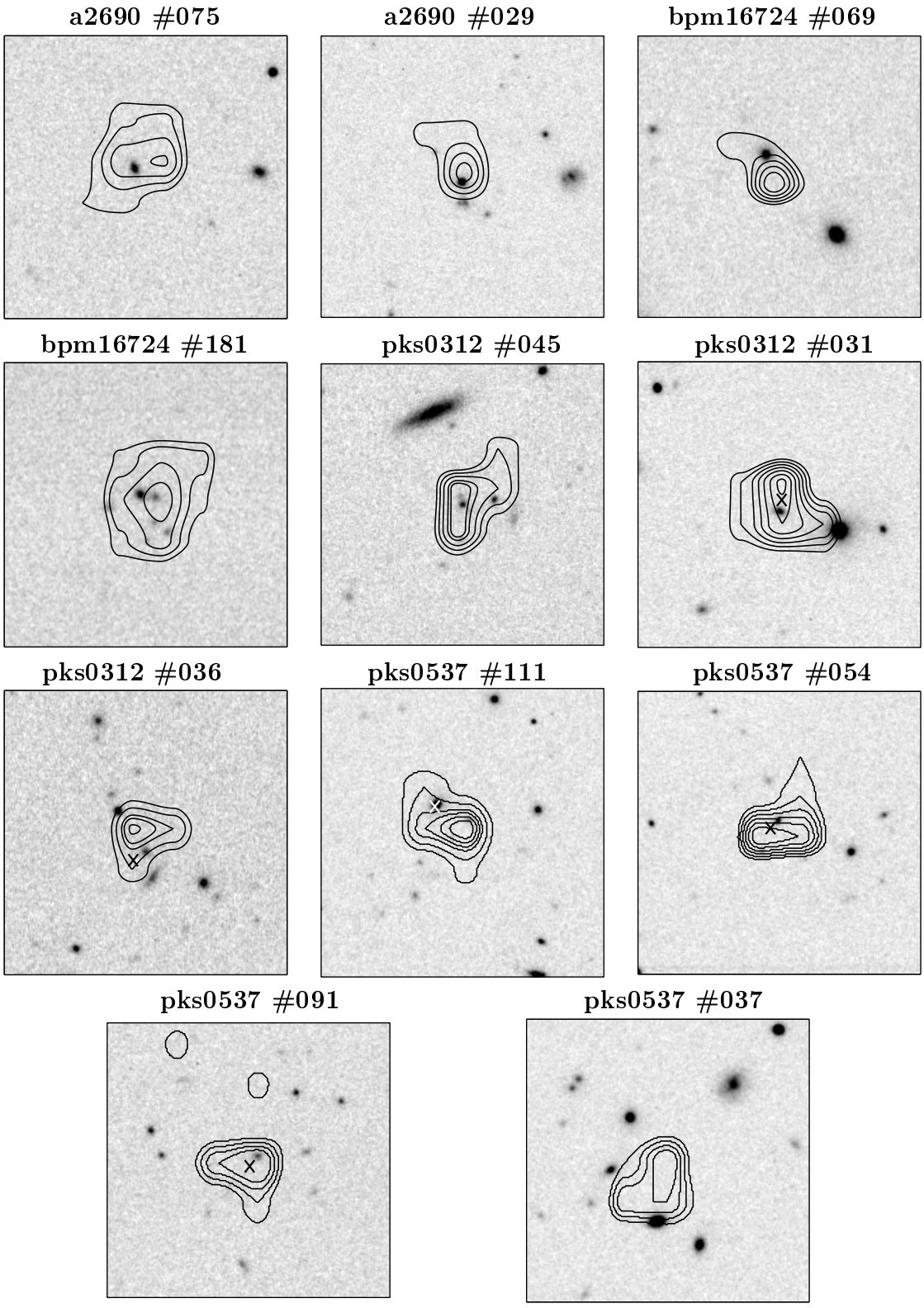

Fig. 2. ISAAC K_s images, centered on the X-ray source centroid and 30″ wide. North is to the top and east to the left. The X-ray contours are overlaid on each image. For 5 objects in the PKS 0312-77 and PKS 0537-28 fields we also show as a small cross the position of the source detected by *Chandra*.

possibility that the true counterpart of this X-ray source might be either heavily reddened (e.g. similar to some AGN-hosting SCUBA galaxies, Ivison et al. 2000) or at very high redshift (Koekemoer et al. 2004).

Table 3. Near infrared properties.

Source Id.	RA(K_s) (J2000)	Dec(K_s) (J2000)	$\Delta(K_s - X)$[a] ($''$)	K_s[b]	$R-K$[c]	P(field)[d]	P(EROs)[e]
Abell 2690 #075	23 59 56.41	−25 10 17.6	3.5	18.32	6.3 ± 0.7	2.2×10^{-2}	1.1×10^{-4}
Abell 2690 #029	00 01 11.50	−25 12 06.5	3.8	17.68	7.4 ± 1.0	1.6×10^{-2}	1.0×10^{-4}
	00 01 11.49	−25 12 08.7	5.9	18.48	>5.9	7.3×10^{-2}	3.0×10^{-4}
BPM 16274 #069	00 50 30.86	−52 00 47.6	2.2	17.83	6.6 ± 0.8	4.2×10^{-3}	3.0×10^{-5}
BPM 16274 #181	00 50 31.51	−52 06 33.9	3.0	18.69	6.2 ± 0.4	2.6×10^{-2}	3.6×10^{-4}
	00 50 31.35	−52 06 34.2	3.8	19.43	>5.3	7.2×10^{-2}	1.4×10^{-2}
PKS 0312-77 #045	03 10 18.93	−76 59 58.4	0.5	18.70	5.7 ± 0.7	6.4×10^{-4}	4.6×10^{-5}
	03 10 17.93	−76 59 57.9	3.6	19.45	>5.5	6.2×10^{-2}	1.2×10^{-2}
PKS 0312-77 #031[f]	03 11 13.65	−76 53 59.6	1.0	18.31	5.3 ± 0.5	1.7×10^{-3}	9.6×10^{-5}
PKS0312-77 #036[f]	03 13 42.90	−76 54 23.9	2.9	19.11	5.5 ± 0.5	3.2×10^{-2}	2.9×10^{-3}
[g]	03 13 43.76	−76 54 19.6	3.5	18.67	2.3 ± 0.2	3.1×10^{-2}	
	03 13 42.68	−76 54 26.7	5.5	18.71	5.1 ± 0.5	7.4×10^{-2}	5.5×10^{-3}
PKS 0537-28 #111[f]	05 39 11.60	−28 37 15.1	3.2	17.66	6.8 ± 0.7	1.1×10^{-2}	9.0×10^{-5}
	05 39 11.35	−28 37 16.7	2.2	20.11	4.6 ± 1.0	3.5×10^{-2}	
PKS 0537-28 #054[f]	05 39 45.22	−28 49 09.8	1.6	18.91	>6.2	8.0×10^{-3}	1.2×10^{-4}
PKS 0537-28 #091[f]	05 40 21.13	−28 50 37.6	1.0	18.99	5.1 ± 0.5	3.3×10^{-3}	4.3×10^{-4}

[a] Positional offset between the near-infrared counterpart and X-ray sources.
[b] "Total" magnitude: MAG_BEST from *SExtractor*.
[c] Fixed 3″-diameter aperture color.
[d] Probability of the galaxy being located near the X-ray source by chance.
[e] Probability of being an Extremely Red Object located near the X-ray source by chance.
[f] Source in the FOV of *Chandra* observations.
[g] Spectroscopically confirmed star, but 4.″8 from the *Chandra* X-ray source.

In five cases more than one object is detected in the K_s band within 6″ from the X-ray centroid. Table 3 gives all the relevant photometric information about the detected counterparts. We decided to adopt a statistical approach to securely identify the near-infrared object responsible for the X-ray emission. For each counterpart detected within 6″ from the X-ray position we computed the probability to find by chance an object within this radius:

$$P = 1.0 - \exp\left(-\pi\Delta^2 n(<K_s)\right), \quad (1)$$

where Δ is the distance between the X-ray and near-infrared sources, and $n(<K_s)$ the integral surface density of galaxies brighter than K_s. If more than one counterpart is present, the most likely candidate is that with the lowest value of P (see Downes et al. 1986, for more details). Two sets of probabilities are reported in Table 3, which were computed assuming the surface density of field galaxies and EROs, respectively. The surface density of field galaxies in the K_s band was determined from our data and without taking into account any color information, whereas for the Extremely Red Objects (with $R-K>5$) we used the results of Daddi et al. (2000) and Roche et al. (2002). In all but one of the cases, where more than one counterpart is present within the X-ray error circle, the brightest K_s counterpart is also the nearest.

Five of our targets in the PKS0312-77 and PKS0537-28 fields were in the field of view of *Chandra* observations. All five sources are clearly detected by a standard detection algorithm (we refer to Brusa et al. 2003 for details on the *Chandra* data reduction). The *Chandra* positions are shown in Fig. 2 with a cross. In all cases, the better positional accuracy of *Chandra* unambiguously points to the reddest, and near-infrared brighter object, with an offset always smaller than 1.″5. Thanks to the excellent position accuracy of *Chandra* observations it was possible to secure the correct identification of the source PKS0312-77 #36, where three objects with similar chance probabilities were found in the XMM-*Newton* error box.

The positional coincidence with the most probable candidate when a *Chandra* observation was available, allowed us to unambiguously elect the most probable candidate as responsible of the hard X-ray emission for all of the sources in the sample.

The presence in four cases of another object with ERO colors (and for one source, BPM 16274 #181, the presence of five EROs within 5″ from the brighter K_s counterpart, indicating a possible high-z cluster), is a natural consequence of the already known clustering properties of these objects (Daddi et al. 2002). We refer to these objects as "secondary" counterparts.

Summarizing, we have positively identified 10 hard X-ray, high X/O sources with relatively bright K_s counterparts; all of them are Extremely Red Objects and most of them (6 out of 10) belong to the extreme tail of the ERO population ($R-K>6$).

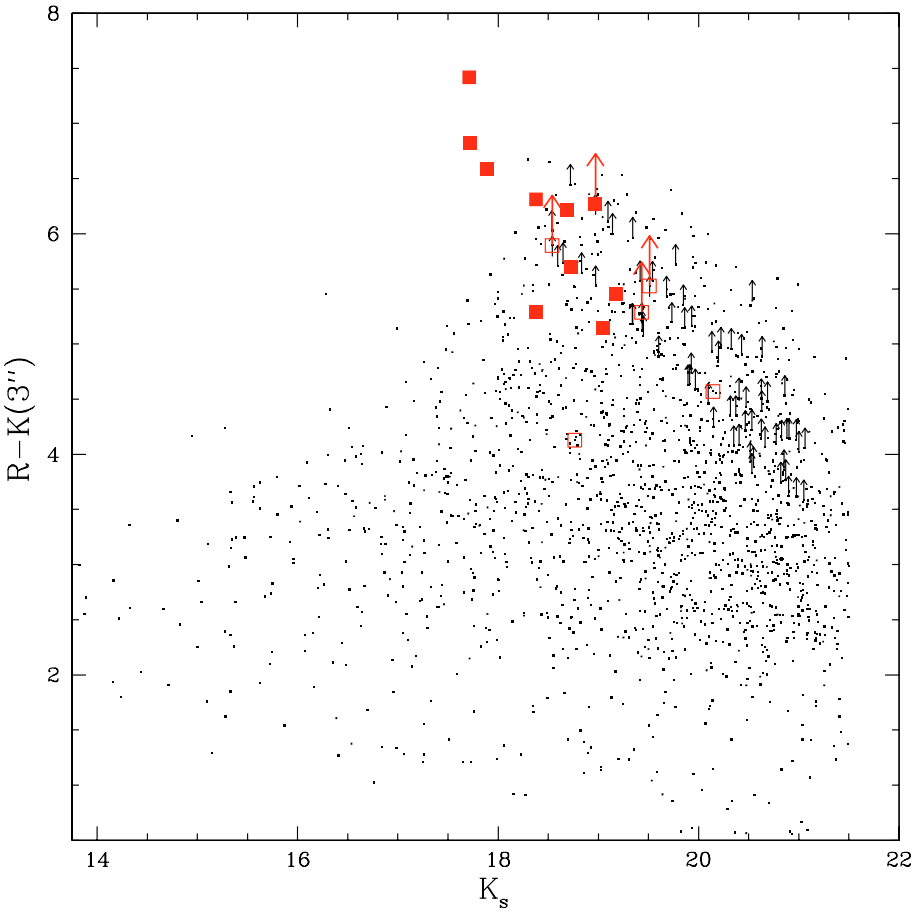

Fig. 3. Fixed-aperture $R - K_s$ color versus "total" K_s magnitude for all the *ISAAC* detections (small dots) with $K_s < 21.5$; the large filled squares indicate the ten counterparts of the selected hard X-ray sources with high X/O. The large empty squares are the "secondary" counterparts.

4.2. Comparison with field population

The $R-K$ color distribution of all of the *ISAAC* detections with $K_s < 21.5$ is shown in Fig. 3. The exceptional nature of the high X/O counterparts is quite obvious: the three brightest counterparts, with $K_s < 18$ *and* $R - K > 6$, are unique with respect to the galaxy field population, as no other object shares the same photometric properties. The six $R - K > 6$ counterparts, with $K_s < 19$, are also very rare objects: in this region of the color-magnitude plane we find 20 galaxies in total, representing a mere 3% of the whole galaxy population[6]. All of the 10 most likely counterparts satisfy the ERO color criterion $R - K > 5$ (and 9 out of 10 also the more stringent limit $R - K \geq 5.3$) and are brighter than $K_s = 19.2$. Given the ERO surface density expected at these magnitude levels (∼1 object per square arcmin, see Daddi et al. 2000; Roche et al. 2002), it is remarkable that we found them nearly ubiquitously in our small error boxes.

The ERO population selected in the optical/near-infrared surveys is known to consist of old, passively evolving ellipticals and star-forming galaxies strongly reddened by dust extinction at high redshift ($z \gtrsim 1$). The two components seem to be about equally represented (see Mannucci et al. 2002 for a tentative photometric separation or Cimatti et al. 2002b for the first spectroscopic classification of an ERO sample). In addition, a few examples of EROs hosting AGN have been discovered so far (Afonso et al. 2001; Pierre et al. 2001). Finally, red quasars with very large optical-to-near infrared colors (up to $R - K \sim 8$) have been discovered in radio surveys (Webster et al. 1995; Lawrence et al. 1995; Gregg et al. 2002).

In order to discriminate among the above mentioned possibilities, and to constrain the source redshift, the exceptional quality of the *ISAAC* images has been fully exploited by combining the photometric information with an accurate morphological analysis.

4.3. Near-infrared morphologies

The morphologies of the near-infrared counterparts were investigated using the IRAF task `isophote`, which fits each galaxy with elliptical isophotes, providing a radial intensity profile along the semi-major axis. With the exception of the identifications of Abell 2690 #029 and PKS 0312−77 #045, all of the other sources are clearly extended.

From the analysis of the radial profiles the half-light radii (r_{hl}) were computed. In a few cases, a nearby object can affect the profile fitting: in these cases we have masked

[6] This fraction is higher than the value (1.7%) found by Daddi et al. (2000) in their larger survey, but we must take into account the fact that our fields can not be considered random fields with respect to the ERO surface density.

Table 4. Near infrared morphological parameters.

Source Id.	K_s[a]	$R-K$[b]	morph[c]	r_{hl}	morph[d]	r_{eff}	gal/nuc[e]
Abell 2690 #075	18.32	6.3 ± 0.7	(E)	0.″56	E	0.″56	>40
Abell 2690 #029	17.68	7.4 ± 1.0	P				
BPM 16274 #069	17.83	6.6 ± 0.8	E/D	0.″60	E	0.″48	>50
BPM 16274 #181	18.69	6.2 ± 0.4	(E)	0.″53	E	0.″37	6.3
PKS 0312-77 #045	18.70	5.7 ± 0.7	P				
PKS 0312-77 #031	18.31	5.3 ± 0.5	D	0.″55	D	0.″47	1.9
PKS 0312-77 #036	19.11	5.5 ± 0.5	(E)	0.″55	E	0.″57	>18
PKS 0537-28 #111	17.66	6.8 ± 0.7	E	0.″61	E	0.″70	33.
PKS 0537-28 #054	18.91	>6.2	E	0.″43	E	0.″48	7.9
PKS 0537-28 #091	18.99	5.1 ± 0.5	E	0.″66	E	0.″80	>25

[a] "Total" magnitude: MAG_BEST from *SExtractor*.

[b] Fixed 3″-diameter aperture color.

[c] From least-square fit: P = point-like – E = Bulge profile – D = Disky profile.

[d] From simulations.

[e] Ratio between the host galaxy and the unresolved nuclear component fluxes.

out the neighbors before carrying out the analysis. A least-square fitting, excluding the inner region affected by the seeing, was performed in order to distinguish between exponential and bulge ($r^{1/4}$) profiles. This straightforward approach, which simply uses r_{hl}, a *measured* model-independent parameter, allowed us to assign a morphological type to all but one of the galaxies. Only for the counterpart of BPM 16274 #069 both the exponential and $r^{1/4}$-law profiles give equally acceptable fits. The good quality of the fits, which use only "canonical" galaxy profiles, is a first clear indication that any contribution from unresolved sources, which would be expected to trace the X-ray emitting AGN, is probably negligible in the extended sources. The results are reported in Table 4.

The half-light radius determination may be biased by several effects. The most important are the seeing blurring and the effect of the surface brightness threshold imposed by the noise ($\sigma_{\mu(k_s)} \approx 22$ mag/arcsec^2; see Table 2) in computing the total magnitude. In order to correct for these effects, and hence to obtain a more reliable measure of the *intrinsic* effective radius of our galaxies, we performed accurate simulations using the `IRAF` task `mkobject`. A grid of models including a point-like source and two sets of bulge and disc (exponential) profiles with a wide range of effective radii and flux ratios between the point-like and the extended components were computed. The simulations were also convolved with the seeing, where the PSF has been modeled with a Moffat function with parameters determined using about 5−10 stars per field. As for the real objects, we use `isophote.ellipse` to extract a radial intensity profile for each model. The model giving the smallest residuals compared to the observed profile (after checking by eye the two-dimensional "object-model" image) is then used to estimate the morphological type, the "seeing-corrected" effective radius, and the possible contribution from an unresolved nuclear component. In the last three columns of Table 4, the best-fit results from the simulations are given, showing an excellent agreement with those of the direct profile fitting: all of the morphological types have been confirmed, and the object with uncertain classification (BPM 16274 #069) is now consistent with an elliptical profile. Moreover, in all but one case the possible contribution from a central, unresolved source is almost negligible ($\lesssim$15%), the only exception being the source PKS 0312−77 #031, a disky galaxy for which the simulations admit the presence of a point-like nucleus, about half as bright as the host galaxy. The best-fitting models superimposed on the near-infrared surface brightness profiles are presented in Fig. 4. The results of the simulations allow us to estimate how the observational biases affect the half-light radius determination: for the exponential profiles[7], the intrinsic effective radius derived from the simulations is always smaller than that measured directly on the images, since these profiles are more prone to seeing blurring. The same behavior is present also in the elliptical hosts observed under the worst seeing conditions (in both the BPM 16274 fields), whereas the intrinsic effective radius is larger than the measured half-light radius for those objects observed in optimal seeing conditions. In the latter case, the dominant observational effect is the light loss in the outermost regions of the galaxy profile, which leads to an underestimate of the total luminosity, thus affecting the half-light radii determination. This effect is due to the surface brightness threshold imposed by the noise, which is known to be more important for the slowly decreasing elliptical profiles (Cimatti et al. 2002a; Angeretti et al. 2002).

5. Discussion

5.1. Redshift constraints

Because of their high X/O ratios and large $R-K$ colors, we argue that most of the sources are likely to be obscured AGN at high redshift. However, the lack of a multi-band coverage does not allow us to estimate a precise photometric redshift.

[7] The simulations included also the "secondary" counterparts of Abell 2690 #029 and PKS 0312−77 #036, and both are disky galaxies.

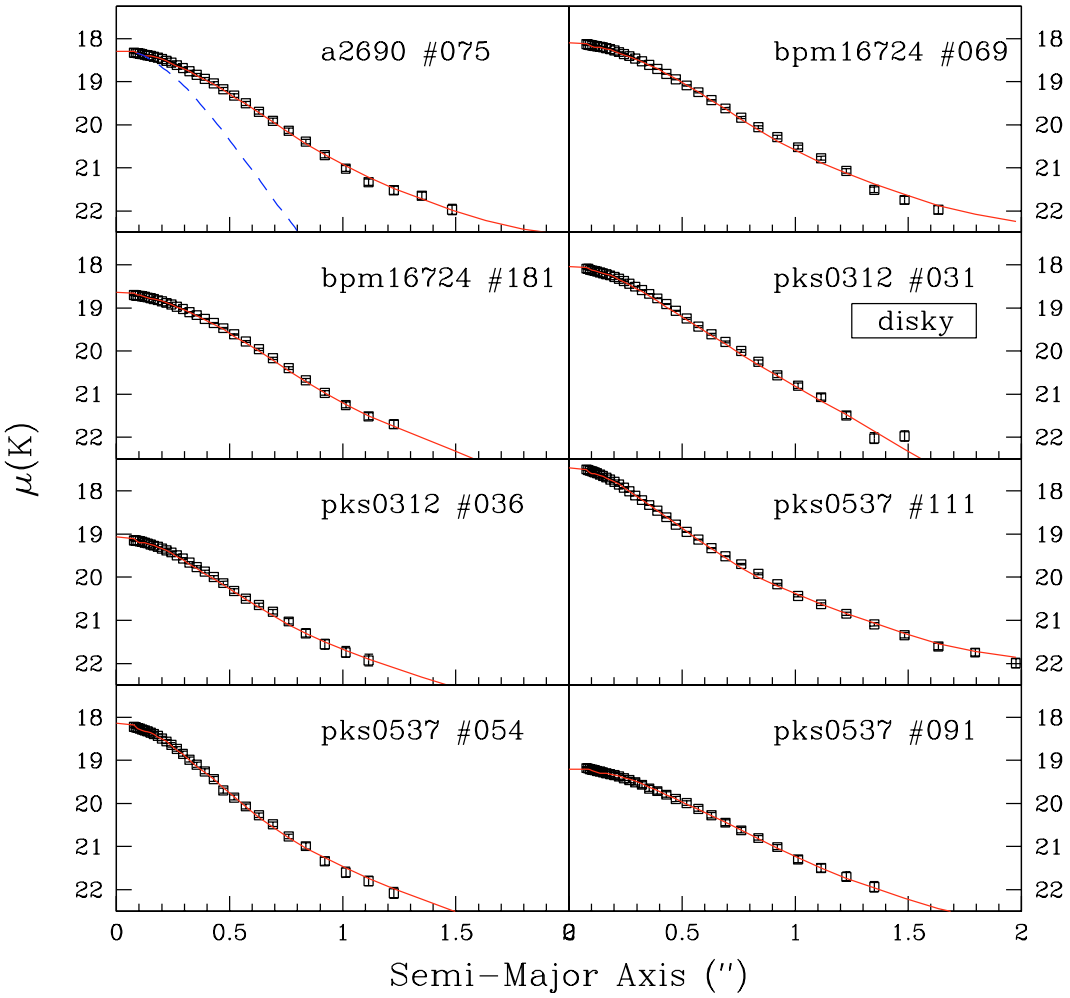

Fig. 4. Surface brightness profiles along the major axis (boxes) and best-fitting models (lines) for all of the extended sources. In the upper left box we also show with a dashed line a representative PSF.

Broad-band photometry in at least 4–6 filters (from U to K) would be needed for a reliable redshift estimate for these objects (Bolzonella et al. 2000)[8]. Nevertheless, we have estimated a "minimum" photometric redshift ($z_{\rm min}$) for all of the sources using the color-redshift diagram ($R-K$ vs. z) and different templates according to their morphology.

In particular for the point-like sources, since the emission from the AGN contributes significantly in the optical/near-IR range, we have used as a QSO template the composite spectrum from the Large Bright Quasar Survey (LBQS; Francis et al. 1991), extended to the near-IR using the mean radio-quiet quasar energy distribution by Elvis (1994; see also Maiolino et al. 2000). Conversely, for extended objects (both bulge and disky morphology, respectively E and D in Table 4) the minimum photometric redshifts are based on the assumption that their optical/near-infrared spectral energy distribution (SED) is due to stellar processes (this assumption is strengthened by the results on the low contribution of point-like nuclei in these counterparts). The adopted templates consist of a set of synthetic spectra from GISSEL 2000 (Bruzual & Charlot 1993), with different star formation histories and spanning a wide range of ages; the basic set of templates includes only solar metallicity and Salpeter's Initial Mass Function (IMF, Salpeter 1955).

In Fig. 5 we show the color-redshift diagram for our two point-like sources (large filled dots) along with data taken from the literature. We have included the optically selected quasar sample with near-IR counterparts in the 2MASS (Barkhouse et al. 2001; small squares), which nicely fits the extended LBQS template. The effect of the intergalactic medium (IGM) attenuation (Madau et al. 1995) is clearly visible at high redshift. Also shown is the 2MASS-selected sample of red quasars from Hutchings et al. (2003) at low redshift (large squares), and the high-z reddest QSOs from Gregg et al. (2002; solid triangles). In order to reproduce the color of red quasars, we have included the effect of internal dust attenuation on the Francis extended template, using a dust-screen model and the SMC extinction law (Pei 1992). The attenuated templates reproduce quite well most of the low-z red quasar sample, as well as the high-z reddest QSOs, with $E(B-V)$ ranging from 0 to 0.7, corresponding to $A_{\rm V} < 2.0$ (see also Gregg et al. 2002). First, we note that most (10 over 13) of observed QSOs with $R-K > 5$ lie at $z > 1$, the only exceptions being one optically selected

[8] We note, however, that due to the extreme faintness of these objects in the UV/optical region, a multi-color observation would be extremely time consuming.

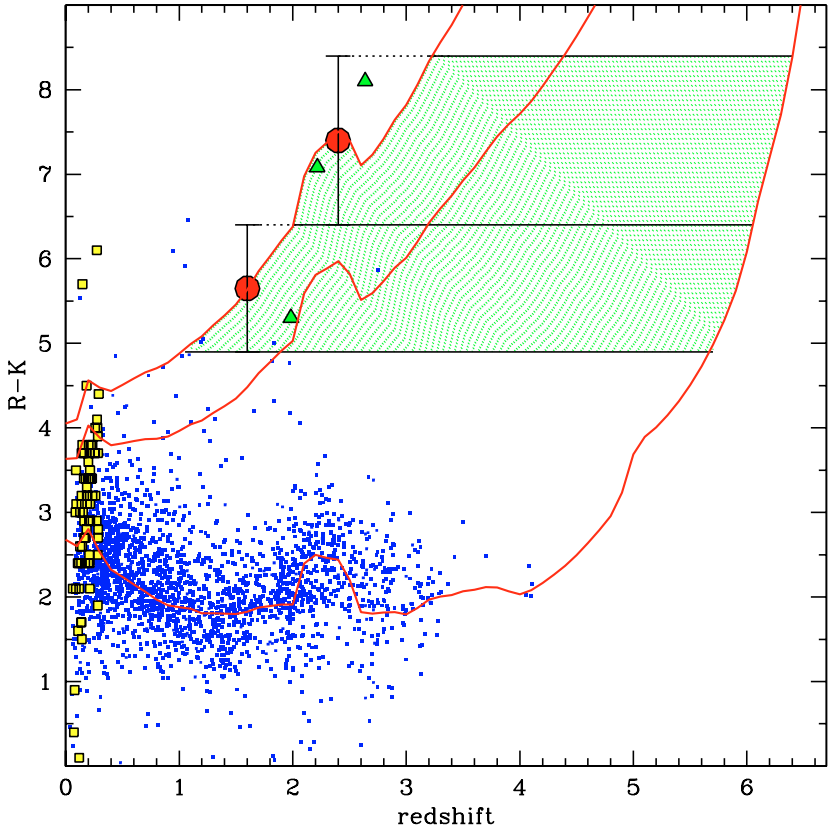

Fig. 5. Redshift vs. optical-to-near infrared color for pointlike objects. The large filled dots represent our point-like sources. The small squares are the optically selected quasars from Barkhouse & Hall (2001), whereas the larger squares indicate the 2MASS quasar sample (Hutchings et al. 2003). The three solid triangles are the high-z reddest QSO from Gregg et al. (2002). The curves represent the color–redshift relations for the adopted quasar template with three different extinction values ($E(B-V) = 0.0, 0.4, 0.7$, from bottom to top). The redshift-permitted region of `Hellas2XMM` sources is shaded.

quasar (Barkhouse et al. 2001) and two 2MASS selected QSOs at $z < 0.3$ (Hutchings et al. 2003). However, the X-ray properties of the low-z 2MASS QSOs are completely different from those of the sources in our sample, having on average very low X/O ratios (Wilkes et al. 2002). Therefore, from the analysis of literature data we could confidently infer that our extremely red point-like sources lie at $z > 1$. In addition, we use the upper envelope of the observed color–redshift diagram for spectroscopically identified QSO, reproduced by an extinction value $E(B-V) \simeq 0.7$ (in agreement with the maximum confirmed AGN extinction to date; Gregg et al. 2002), to estimate the minimum redshift for a given $R-K$ color. We can thus assert, with good confidence, that the two point-like sources in our sample are at $z > 1$ and derive their $z_{\rm min}$ (see Table 5). The observed colors correspond to $z_{\rm min} = 1.65^{+0.35}_{-0.65}$ for PKS 0312−77 #045 and $z_{\rm min} = 2.40^{+0.90}_{-0.40}$ for Abell 2690 #029A. The rest-frame de-reddened luminosities in the B[9] and $K_{\rm s}$ bands are consistent with the optical and near-IR luminosity distributions in the Barkhouse et al. (2001) sample ($\langle M_B \rangle = -26.3$, $\sigma(M_B) = 2.2$ and $\langle M_K \rangle = -29.4$, $\sigma(M_K) = 1.9$). Finally, from the unattenuated QSO template, we can also place a limit to the maximum redshift of point-like sources (see Fig. 5). Indeed, assuming that their extremely red colors are due to the high-z IGM absorption, their maximum redshift is around $z = 6$–6.5. In this case the luminosities derived from the near-IR are typically 1–1.5 mag brighter than in $z_{\rm min}$ case.

With a similar procedure we have estimated a $z_{\rm min}$ for sources with a bulge or disky profile. For the bulge-profile sources we have used for comparison the sub-sample of early-type galaxies in the K20 spectroscopic survey (Cimatti et al. 2002a). In Fig. 6 we show the model which best represents the upper envelope of the K20 data of early-type galaxies, which is computed assuming a simple stellar population forming at high redshift ($z_{\rm form} = 20$). It corresponds to a "maximum age" model and provides the reddest colors at each redshift. A lower $z_{\rm form}$ and/or a more gradual star formation history would result in bluer colors and in a corresponding higher $z_{\rm min}$. For the disky sources we have used for comparison the sub-sample of emission-line galaxies of the K20 survey. To reproduce the colors of the most extreme emission-line dusty objects we have chosen a model with constant Star-Formation Rate (SFR), and

[9] the effect of the dust in the B-band is about 2.6 mag for $E(B-V) = 0.7$.

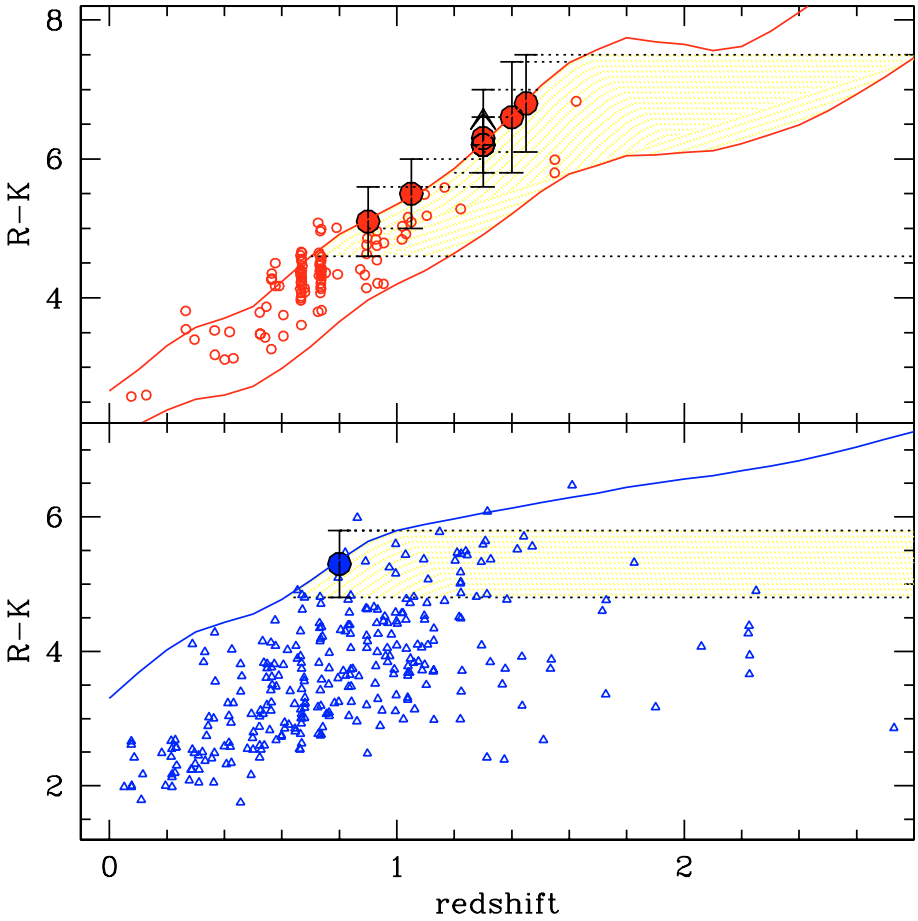

Fig. 6. Redshift vs. optical-to-near infrared color for extended objects. The large filled symbols represent the `Hellas2XMM` sources. The smaller empty symbols are sources from the K20 spectroscopic survey (Cimatti et al. 2002a). In the upper panel we compare our bulge profile sources with the K20 early-type galaxies. In the lower panel we compare the disky sources with a sample of emission line galaxies. In both panels also the "maximum color – minimum redshift" track (see text) is shown. The redshift-permitted region of `Hellas2XMM` sources is shaded.

a SMC extinction law with $E(B-V) = 0.6$ (cf. Cimatti et al. 2002a; Pozzetti et al. 2003). We have then assigned a $z_{\rm min}$ to each of our sources according to their $R-K$ color and morphological type.

We found that the minimum redshifts for bulge and disky profile sources are in the range of $0.80 \leq z \leq 1.45$. In Table 5 we list the $z_{\rm min}$ and their color-related uncertainties. Also reported are the intrinsic rest–frame luminosities in the B and $K_{\rm s}$ bands. We note that most of the extended sources are more than 1 mag brighter than typical local L^*_K galaxies ($M^*_{K_{\rm s}} = -24.21$ at $z = 0$ from Cole et al. 2001) and similar or even brighter than L^*_K galaxies at $z = 1-1.5$ (Pozzetti et al. 2003). Taking into account that the $M_{\rm stars}/L_K$ ratio for an old stellar population could vary from 0.3 (for an age of 1 Gyr, assuming a Salpeter IMF) to about 1 (for 6 Gyrs, the age of the universe at $z = 0.9$), we estimate the galaxy stellar Masses of our hosts: they are all above $3 \times 10^{10}\ M_\odot$ (and 4 of them above $10^{11}\ M_\odot$), corresponding to the stellar-Mass of an L^* galaxy in the local Universe (Cole et al. 2001). The elliptical hosts of hard X-ray sources with extreme X/O are therefore among the most massive spheroids at these redshifts, possibly addressing the issue of elliptical galaxy formation and the expected co-evolution with the black-hole accretion (Granato et al. 2001).

The procedure above described leaves the maximum redshifts basically unconstrained. However, we can infer $z_{\rm max}$ for bulge sources assuming a lower bound to the observed K20 data, represented by an old stellar population with an age of 1 Gyr, consistent also with their relaxed morphological properties. The expected range in redshift ($z_{\rm min} - z_{\rm max}$) is shown by the shaded area in Fig. 6.

5.2. Angular sizes of the EROs

In Sect. 4.3 we have shown that our accurate morphological profile analysis has allowed us to measure the effective angular radius for the extended sources. First of all, we note that their angular sizes are in general quite small, ranging from 0.5″ to 0.8″, and therefore consistent with being high-z objects. For a small sample of X-ray selected EROs, Stevens et al. (2003) found similar or even smaller angular radii. Assuming the minimum redshift computed above, we have derived the intrinsic dimension for each extended source, listed in Table 5. The intrinsic effective radii are in the range $3.1 < r_{\rm eff} < 6.2$ kpc, similar to that of local L^* galaxies.

Table 5. Minimum redshifts and intrinsic rest-frame properties.

Id.	morph	$z_{\rm min}$	M_K	M_B	$r_{\rm e}$ (kpc)	$N_{\rm H}$ (10^{22} cm^{-2})	$L_{2-10\ {\rm keV,unabs}}$ (10^{44} erg s^{-1})
Abell 2690 #075	E	$1.30^{+0.20}_{-0.20}$	−25.83	−21.77	4.7	$15.3^{+23.2}_{-\ 9.1}$	3.5
Abell 2690 #029	P	$2.40^{+0.90}_{-0.40}$	−29.74	−26.31[a]	–	$2.8^{+\ 3.5}_{-\ 2.1}$	11.2
BPM 16274 #069	E	$1.40^{+0.20}_{-0.20}$	−26.53	−22.49	4.1	$2.6^{+\ 1.6}_{-\ 1.1}$	3.6
BPM 16274 #181	E	$1.30^{+0.10}_{-0.10}$	−25.45	−21.40	3.1	$1.1^{+\ 3.2}_{-\ 1.0}$	1.2
PKS 0312-77 #045	P	$1.65^{+0.35}_{-0.65}$	−28.02	−24.58[a]	–	$6.6^{+\ 7.4}_{-\ 3.8}$	4.9
PKS 0312-77 #031	D	$0.80^{+0.20}_{-0.20}$	−24.77	−22.10[b]	3.5	$1.2^{+\ 1.2}_{-\ 0.8}$	0.5
PKS 0312-77 #036	E	$1.05^{+0.20}_{-0.20}$	−24.44	−20.33	4.6	$1.2^{+\ 1.5}_{-\ 1.0}$	1.0
PKS 0537-28 #111	E	$1.45^{+0.20}_{-0.20}$	−26.80	−22.77	5.9	$12.0^{+16.6}_{-\ 7.2}$	2.8
PKS 0537-28 #054	E	>1.30	−25.24	−21.18	4.0	$1.6^{+\ 2.4}_{-\ 1.2}$	>1.6
PKS 0537-28 #091	E	$0.90^{+0.20}_{-0.20}$	−24.17	−20.01	6.2	$15.7^{+49.9}_{-11.2}$	2.0

[a] de-reddened by 2.6 mag assuming $E(B-V) = 0.7$.
[b] de-reddened by 2.3 mag assuming $E(B-V) = 0.6$.

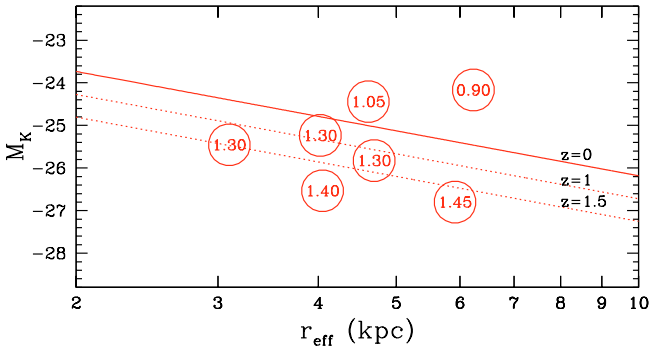

Fig. 7. Effective radius vs. luminosity relation for extended objects with a bulge profile. Objects are identified by their $z_{\rm min}$. The solid line shows the local relation from Pahre et al. (1998), while the dotted lines show its evolution at $z = 1$ and $z = 1.5$, assuming the luminosity evolution derived by Pozzetti et al. 2003.

In Fig. 7 we show the absolute $K_{\rm s}$-band magnitude vs. intrinsic effective radius for bulge sources, compared with the relation between luminosity and radius derived from the local sample of Pahre et al. (1998) in the near-IR (Angeretti et al. 2002). Our sources do not follow the local luminosity-radius relation, most of them (5/7) being more luminous or smaller than observed locally at a given radius or luminosity, respectively. A decrease of the intrinsic galaxy dimensions at high-z has been suggested also by Trujillo et al. (2003). On the other hand, in Fig. 7 we show the same local relation shifted at $z = 1,\ 1.5$ assuming the luminosity brightening derived in the K20 survey by Pozzetti et al. (2003) with no change in the light profiles. Such a luminosity brightening could explain the observed radii for the sources at $z \geq 1.3$. The discrepancy between the observed and expected luminosity for the two objects at the lowest redshifts suggests that these sources have a higher redshift than the adopted (minimum) one. Indeed, assuming higher-z would move the sources in Fig. 7 essentially vertically toward brighter luminosities, because of the small redshift dependence of the intrinsic size at $z > 1$.

Concluding, the analysis of the luminosity-radius relation is consistent with the color-based estimates for the minimum redshift of our high X/O, hard X-ray selected sources.

5.3. X-ray properties of high X/O EROs

The X-ray spectra of all ten high X/O sources have been fitted with a single power law model plus absorption in the source rest-frame assuming for all of them the "minimum" redshift estimated in the previous section. The quality of the X-ray spectra in terms of S/N ratio is not such to simultaneously constrain both the slope and column density. For this reason the former was fixed at $\Gamma = 1.9$, the average value obtained by fitting the "bright" part of the `Hellas2XMM` sample (see Perola et al. (in preparation) for a detailed description of the spectral analysis procedures). The best-fit values for the intrinsic column densities and unabsorbed X-ray luminosities are listed in Table 5. All of the sources in our sample have a best-fit $N_{\rm H}$ larger than 10^{22} cm^{-2}, and for half of them also the 90% lower limits are consistent with significant X-ray absorption.

For three objects in our sample (the two point-like objects and the disky galaxy) we estimated both the optical reddening and the X-ray absorbing column density; we calculated the $E_{B-V}/N_{\rm H}$ ratio and we found it significantly lower than the Galactic standard value (1.7×10^{-22} mag cm^2, Bohlin et al. 1978). The $E_{B-V}/N_{\rm H}$ is lower by a factor of ∼10 for the point-like sources PKS 0312−77 #045 and Abell2690 #029A, whereas for the disky galaxy the ratio is at least three times lower than the Galactic one. This confirms the results for X-ray selected AGN (see Maiolino et al. 2001 and references therein), for which there is increasing evidence that the AGN circumnuclear region has different dust properties than the Galactic diffuse interstellar medium.

The unabsorbed 2–10 keV X-ray luminosities of all but two of the objects in the `Hellas2XMM` are larger than 10^{44} erg s^{-1}. The presence of more than one object with ERO colors around the most probable counterpart suggests that the X-ray emission could be due to a cluster of galaxies which remains unresolved with XMM-*Newton*. While the observed X-ray luminosities would be consistent with this possibility (Rosati et al. 2002), the observed spectra are much harder than expected from the intracluster medium thermal emission at the estimated redshifts. Moreover, the *Chandra* X-ray fluxes, when available, are consistent with the XMM ones, indicating that these X-ray sources are probably point-like. The majority of our relatively

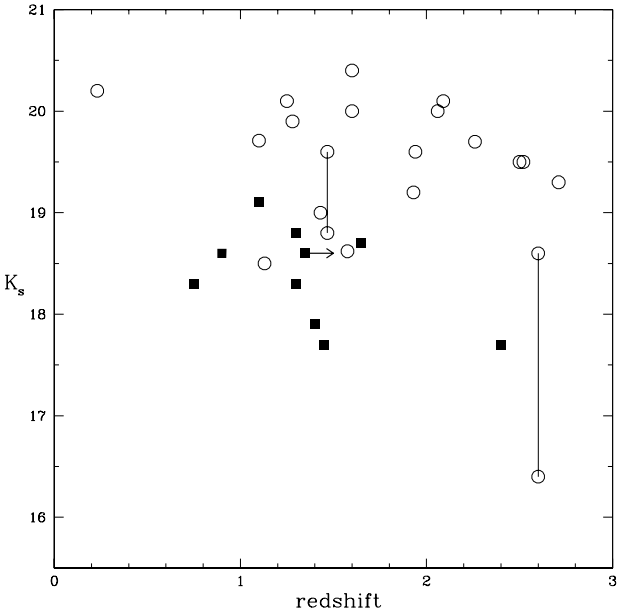

Fig. 8. Redshift vs. K_s magnitude for our targets (filled square) and for a comparison sample of high X/O sources with ERO colors extracted from the literature (empty circles; see text). The two pairs of connected circles represent two lensed objects in the Abell 2390 field (Crawford et al. 2001) with observed and de-magnified K_s.

bright hard X-ray selected sources with high X/O and ERO colors are therefore obscured, high-luminosity AGN, i.e., type II quasars (see also Fiore et al. 2003) .

In order to check whether the X-ray absorption is common among this type of objects we have built a comparison sample of high X/O sources with ERO colors serendipitously discovered at X-ray fluxes comparable to those of our sample. We have considered only those X-ray sources for which a reliable spectroscopic or photometric identification was available in the literature: #19 and #25 in the Lockman Hole (Mainieri et al. 2002; see also Stevens et al. 2003); A15 and A18 in A2390 field (Crawford et al. 2001; Gandhi et al. 2002); N2_21 and N2_28 in the ELAIS survey (Willott et al. 2003). All but one (N2_21) of the objects in the comparison sample have column densities in excess of 10^{22} cm^{-2}, in agreement with the results obtained for the Hellas2XMM sample.

At fainter X-ray fluxes, sources with extremely high X-ray-to-optical flux ratios have been also discovered in the deep pencil-beam surveys. From the Barger et al. (2003) catalog of the 2 Ms CDF-N observation, we have selected all of the objects with X/O > 10 and $R - K > 5$; among these, 13 sources have a spectroscopic or photometric redshift. For the two brightest sources absorption column densities in excess of 10^{23} cm^{-2} were derived through proper spectral analysis (see Civano et al. in prep.); in all but one of the remaining cases, the intrinsic column densities inferred from the Hardness-Ratio technique are in excess of 10^{22} cm^{-2} (see also Alexander et al. (2002) for the 1 Ms CDF-N observation). Figure 8 shows that all but one of the 19 sources in the comparison samples lie in the same redshift range derived for Hellas2XMM sources, thus reinforcing the reliability of our method for the redshift determination.

Deep HST ACS observations of a small sample of 7 *Chandra* sources in the CDF-S with extremely high X/O and red colors (EXOs: Extreme X-ray-to-Optical ratio sources) have been recently discussed by Koekemoer et al. (2004). None of them was detected down to very faint optical magnitudes ($z(850) \simeq 28$), although these sources are clearly detected in the K_s band ($K_{vega} \simeq 20.4$–23). It has been proposed that these sources could be high-redshift ($z > 6$) L^* galaxies powered by a moderately luminous AGN ($L_X = 2{-}6 \times 10^{44}$ erg s^{-1}). If they were at lower redshifts, they would be unusually underluminous galaxies. The *Chandra* EXOs could then constitute the high–redshift tail of a population of obscured AGN which is sampled at lower redshifts by the Hellas2XMM high X/O sources. The relatively soft X-ray spectra of *Chandra* EXOs, as inferred from their Hardness-Ratio distribution, would also be consistent with a high-z hypothesis.

6. Summary and conclusion

The most important results obtained from the analysis of high quality near-infrared images of hard X-ray sources with X/O > 10 can be summarized as follows:

1. We have identified 10 out of the 11 Hellas2XMM sources observed with ISAAC at VLT with a relatively bright near infrared ($K_s < 19.2$) counterpart.
2. All of them fall in the class of Extremely Red Objects ($R - K > 5$) and 9 out of 10 satisfy the more stringent criterion $R - K > 5.3$. The trend of finding redder sources at fainter optical magnitudes, as well as an increasing fraction of EROs, are well established results by various X-ray surveys. However, the three brightest counterparts, with $K_s < 18$ *and* $R - K > 6$, are very rare objects also with respect to the galaxy field population and, to our knowledge, objects like these were never found by any other X-ray survey.
3. We found an ERO overdensity around the Hellas2XMM source BPM 16274 #181. Five near-infrared sources with $R - K > 5$ (plus another bluer object) lie within a radius of about 6″ from the hard X-ray source, suggesting the presence of a possible high-z cluster/group of galaxies.
4. Thanks to the excellent observing conditions it was possible to perform an accurate analysis of the surface brightness profiles and provide a morphological classification. Only two objects are classified as point-like sources, while all of the others are extended, without any evidence of a central unresolved nuclear source. The morphological breakdown is dominated by elliptical profiles; only in one case the fit with an exponential law (disky galaxy) provides a better description of the data.
5. We provide a fairly robust estimate of the minimum redshift for each source by comparing the color and morphological information with that available in the literature for spectroscopically identified sources and with models for the spectral energy distribution. The $R - K$ color of the two point-like objects is well matched by a quasar template reddened by dust at $z \simeq 2$. The minimum redshift for extended sources is in the range $z = 0.80$–1.45.

6. Most of the sources in the Hellas2XMM sample show substantial intrinsic absorption in their X-ray spectra. A detailed comparison with X-ray selected sources in various deep and medium–deep surveys indicates that heavy obscuration is almost ubiquitous among objects with high X/O and extremely red colors. All but one of the sources have unabsorbed X-ray luminosities $L_{2-10\,\mathrm{keV}} \geq 10^{44}$ erg s^{-1}, and therefore belong to the type II quasar population. We wish to stress that the seven elliptical galaxies, with no evidence of a central spike, represent, in the whole Hellas2-XMM 1df sample, around 10% of the 72 sources with $L_{\mathrm{x}} \geq 10^{44}$ erg s^{-1}. Thus, a non-negligible fraction of the most luminous AGN, although not heavily obscured (i.e. Compton-thick) in the hard X-ray band, would be missed in UV/optical as well as in near-infrared quasar surveys (see also Gandhi et al. 2004).

Finally, we wish to stress that near–infrared observations of hard X-ray sources selected on the basis of a high X/O ratio have proven to be a powerful technique aimed at studying the hosts of high-z type II AGN, whose obscured nuclei do not affect the host galaxy morphologies. Moreover, our results do indicate that X-ray surveys constitute an efficient mean to select high-redshift, massive elliptical galaxies and that the "obscured" nuclear activity takes place within otherwise normal galaxies, which already formed the bulk of their stars at high redshift. Deep near-infrared spectroscopy of these sources would allow to test this possibility further.

Acknowledgements. We are grateful to G. Zamorani for insightful discussions and to R. Sancisi e M.G. Stirpe for their careful reading of the paper. We thanks the K20 team for making their spectroscopic results available before publication. This work was partially supported by the Italian Space Agency (ASI) under grants I/R/073/01 and I/R/057/02 and by INAF (grant #270/2003).

References

Afonso, J., Mobasher, B., Chan, B., & Cram, L. 2001, ApJ, 559, L101
Alexander, D. M., Vignali, C., Bauer, F. E., et al. 2002, AJ, 123, 1149
Alexander, D. M., Bauer, F. E., Brandt, W. N., et al. 2003, AJ, 126, 539
Angeretti, L., Pozzetti, L., & Zamorani, G. 2002, A New Era in Cosmology, ASP Conf. Proc., 283, 135
Baldi, A., Molendi, S., Comastri, A., et al. 2002, ApJ, 564, 190
Barkhouse, W. A., & Hall, P. B. 2001, AJ, 121, 2843
Barger, A. J., Cowie, L. L., Capak, P., et al. 2003, AJ, 126, 632
Bershady, M. A., Lowenthal, J. D., & Koo, D. C. 1998, ApJ, 505, 50
Bertin, E., & Arnouts, S. 1996, A&A, 117, 393
Bohlin, R. C., Savage, B. D., & Drake, J. F. 1978, ApJ, 224, 132
Bolzonella, M., Miralles, J.-M., & Pello', R. 2000, A&A, 363, 476
Brusa, M., Comastri, A., Mignoli, M., et al. 2003, A&A, 409, 65
Bruzual, A. G., & Charlot, S. 1993, ApJ, 405, 538
Cimatti, A., Daddi, E., Mignoli, M., et al. 2002a, A&A, 381, L68
Cimatti, A., Mignoli, M., Daddi, E., et al. 2002b, A&A, 392, 395
Cole, S., Norberg, P., Baugh, C. M., et al. 2001, MNRAS, 326, 255
Comastri, A., Mignoli, M., Ciliegi, P., et al. 2002, ApJ, 571, 771
Crawford, C. S., Fabian, A. C., Gandhi, P., et al. 2001, MNRAS, 324, 427
Daddi, E., Cimatti, A., Pozzetti, L., et al. 2000, A&A, 361, 535
Daddi, E., Cimatti, A., Broadhurst, T., et al. 2002, A&A, 384, L1
Downes, A. J. B., Peacock, J. A., Savage, A., & Carrie, D. R. 1986, MNRAS, 218, 31
Elvis, M., Wilkes, B. J., McDowell, J. C., et al. 1994, ApJS, 95, 1
Fiore, F., Brusa, M., Cocchia, F., et al. 2003, A&A, 409, 79
Francis, P. J., Hewett, P. C., Foltz, C. B., et al. 1991, ApJ, 373, 465
Gandhi, P., Crawford, C. S., & Fabian, A. C. 2002, MNRAS, 337, 781
Gandhi, P., Crawford, C. S., Fabian, A. C., & Johnstone, R. M. 2004, MNRAS, 348, 529
Giacconi, R., Rosati, P., Tozzi, P., et al. 2001, ApJ, 551, 624
Giacconi, R., Zirm, A., Wang, J. Xi., et al. 2002, ApJS, 139, 369
Gilli, R. 2003, in New X-ray Results from Clusters of Galaxies and Black Holes, ed. C. Done, E. M. Puchnarewicz, & M. J. Ward, in press [arXiv:astro-ph/0303115]
Granato, G. L., Silva, L., Monaco, P., et al. 2001, MNRAS, 324, 757
Green, P. J., Silverman, J., Cameron, R., et al. 2004, ApJS, 150, 43
Gregg, M. D., Lacy, M., White, R. L., et al. 2002, ApJ, 564, 133
Koekemoer, A. M., Alexander, D. M., Bauer, F. E., et al. 2004, ApJ, 600, L123
Hall, P. B., & Green, R. F. 1998, ApJ, 507, 558
Harrison, F. A., Eckart, M. E., Mao, P. H., et al. 2003, ApJ, 596, 944
Hasinger, G., Altieri, B., Arnaud, M, et al. 2001, A&A, 365, L45
Hasinger, G., & the CDF-S team 2003, AIP Conf. Proc., 666, 227 [arXiv:astro-ph/0302574]
Hutchings, J. B., Maddox, N., Cutri, R. M., & Nelson, B. O. 2003, AJ, 126, 63
Ivison, R. J., Smail, I., Barger, A. J. et al. 2000, MNRAS, 315, 209
Lawrence, C. R., Elston, R., Januzzu, B. T., & Turner, E. L. 1995, AJ, 110, 2570
Lehmann, I., Hasinger, G., Schmidt, M., et al. 2001, A&A, 371, 833
Maccacaro, T., Gioia, I. M., Wolter, A., Zamorani, G., & Stocke, J. T. 1988, ApJ, 326, 680
Madau, P. 1995, ApJ, 441, 18
Mainieri, V., Bergeron, J., Hasinger, G., et al. 2002, A&A, 393, 425
Maiolino, R., Salvati, M., Antonelli, L. A., et al. 2000, A&A, 335, L47
Maiolino, R., Marconi, A., Salvati, M., et al. 2001, A&A, 365, 28
Mannucci, F., Pozzetti, L., Thompson, D., et al. 2002, MNRAS, 329, L57
Moorwood, A. F. M., Cuby, J.-G., Ballester, P., et al. 1999, The Messenger, 95, 1
Moustakas, L. A., Davis, M., Graham, J. R., et al. 1997, ApJ, 475, 445
Mushotzky, R. F., Cowie, L. L., Barger, A. J., & Arnaud, K. A. 2000, Nature, 404, 459
Pahre, M. A., Djorgovski, S. G., & de Carvalho, R. R. 1998, AJ, 116, 1591
Pei, Y. C. 1992, ApJ, 395, 130
Persson, E., Murphy, D. C., Krzeminski, W., et al. 1998, AJ, 166, 2475
Pierre, M., Lidman, C., Hunstead, R., et al. 2001, A&A, 372, L45
Pozzetti, L., Cimatti, A., Zamorani, G., et al. 2003, A&A, 402, 837
Roche, N. D., Almaini, O., Dunlop, J., et al. 2002, MNRAS, 337, 1282
Rosati, P., Borgani, S., & Norman, C. 2002, ARA&A, 40, 539
Salpeter, E. E. 1955, ApJ, 121, 161
Saracco, P., Giallongo, E., Cristiani, S., et al. 2001, A&A, 375, 1
Schlegel, D. J., Finkbeiner, D. P., & Davis, M. 1998, AJ, 500, 525
Stevens, J. A., Page, M. J., Ivison, R. J., et al. 2003, MNRAS, 342, 249
Trujillo, I., Rudnick, G., & Rix, H.-W. 2003, ApJ, submitted [arXiv:astro-ph/0307015]
Yan, H., Windhorst, R. A., Röttgering, H. J. A., et al. 2003, ApJ, 585, 67
Webster, R. L., Francis, P. J., Peterson, B. A., et al. 1995, Nature, 375, 469
Wilkes, B. J., Schmidt, G. D., Cutri, R. M., et al. 2002, ApJ, 564, L65
Willott, C. J., Simpson, C., Almaini, O., et al. 2003, MNRAS, 339, 397
Zamorani, G., Mignoli, M., Hasinger, G., et al. 1999, A&A, 346, 731